



SERS spectroscopy using Au-Ag nanoshuttles and hydrophobic paper-based Au nanoflower substrate for simultaneous detection of dual cervical cancer-associated serum biomarkers

Dan Lu^{1,2,3} · Menglin Ran^{1,2} · Yifan Liu^{1,2} · Ji Xia^{1,2} · Liyan Bi⁴ · Xiaowei Cao^{1,2,3,5,6}

Received: 19 May 2020 / Revised: 17 July 2020 / Accepted: 22 July 2020 / Published online: 31 July 2020
© Springer-Verlag GmbH Germany, part of Springer Nature 2020

Abstract

Ultrasensitive detection of specific biomarkers in clinical serum is helpful for early diagnosis of cervical cancer. In this paper, a surface-enhanced Raman scattering (SERS)-based immunoassay was developed for the simultaneous determination of squamous cell carcinoma antigen (SCCA) and osteopontin (OPN) in cervical cancer serum. Au-Ag nanoshuttles (Au-AgNSs) as SERS tags and hydrophobic filter paper-based Au nanoflowers (AuNFs) as capture substrate were constructed into a sandwich structure which served as an ultrasensitive SERS-based immunoassay platform. Finite difference time domain simulation confirmed that the electromagnetic field coupled between the AuNFs had a prominent SERS signal enhancement effect, which improved the detection sensitivity. SERS mapping showed that hexadecenyl succinic anhydride hydrophobic treatment could prevent the analyte from being quickly absorbed by the filter paper and increase the retention time to be more evenly distributed on the filter paper substrate. The immunoassay platform was verified to have good selectivity and reproducibility. With this method, the detection limits of SCCA and OPN in human serum were as low as 8.628 pg/mL and 4.388 pg/mL, respectively. Finally, in order to verify the feasibility of its clinical application, the serum samples of healthy subjects; cervical intraepithelial neoplasia I (CINI), CINII, and CINIII; and cervical cancer patients were analyzed, and the reliability of the results was confirmed by enzyme-linked immunosorbent assay experiments. The constructed SERS-based immunoassay platform could be used as a clinical tool for early screening of cancers in the future.

Keywords Surface-enhanced Raman scattering · Au-Ag nanoshuttles · Au nanoflowers · Cervical cancer · Squamous cell carcinoma antigen · Osteopontin

Electronic supplementary material The online version of this article (<https://doi.org/10.1007/s00216-020-02843-x>) contains supplementary material, which is available to authorized users.

✉ Dan Lu
ludan1968@126.com

✉ Xiaowei Cao
cxw19861121@163.com

¹ Department of Obstetrics and Gynecology, College of Clinical Medicine, Yangzhou University, Yangzhou, China

² The First Clinical College, Dalian Medical University, Dalian, China

³ Jiangsu Key Laboratory of Integrated Traditional Chinese and Western Medicine for Prevention and Treatment of Senile Diseases, Yangzhou University, Yangzhou, China

⁴ Transformative Otology and Neuroscience Center, College of Special Education, Binzhou Medical University, Yantai 264003, China

⁵ Institute of Translational Medicine, Medical College, Yangzhou University, Yangzhou, China

⁶ Jiangsu Co-innovation Center for Prevention and Control of Important Animal Infectious Diseases and Zoonoses, College of Veterinary Medicine, Yangzhou University, Yangzhou 225009, China

Introduction

Every year, more than 500,000 women are diagnosed with cervical cancer worldwide; what's more, about 300,000 women die from this disease [1]. More than 90% of the death comes from developing countries [2, 3]. Meanwhile, the mortality rate of cervical cancer in poor areas in developed countries is twice of that in rich areas [4]. In the early stage of cervical cancer, the 5-year survival rate of patients who take effective treatment (surgery, chemotherapy, etc.) is as high as 90%, while the average survival rate of patients in the late stage is about 25% [1, 2, 5–7]. Therefore, early screening of cervical cancer is particularly important [2]. In addition, developing an early detection method with low price, simple operation, and high specificity can benefit more women in developing countries. Several studies have shown that early detection of tumors can be achieved by detecting tumor-associated antigens in the serum of patients without obvious symptoms [5, 7, 8]. Squamous cell carcinoma accounts for about 80% of cervical cancer [3, 9], so squamous cell carcinoma antigen (SCCA) can be regarded as one of the target antigens for cervical cancer detection. In order to improve detection efficiency, save detection costs, and increase detection accuracy [10], osteopontin (OPN) was selected as another target antigen [11]. OPN not only promotes the malignant development of tumor but also enhances the invasive ability of tumor cells [12, 13]. Some teams have reported that if the content of OPN in human serum increases, it indicates that there may be a tumor in the body or that the tumor is developing [11, 14, 15]. The current methods for detecting tumor-associated antigens include enzyme-linked immunosorbent assay (ELISA), polymerase chain reaction (PCR), localized surface plasmon resonance (LSPR), and chemiluminescence immunoassay (CLIA) [5–7, 11, 16]. Due to the high testing costs, complicated operations, and harsh reaction conditions, these methods cannot be widely used clinically.

The surface-enhanced Raman scattering (SERS) technology has the advantages of rapid detection, high sensitivity, and good selectivity. It can achieve quantitative analysis of specific substances such as nucleic acids, harmful substances, and protein molecules [17–21]. The SERS spectrum has narrow peaks and strong specificity, which can minimize the overlap of spectral lines between different labeled molecules, while collecting Raman spectra of different target analytes [8, 10, 17]. The measured SERS signal intensity can reflect the analyte content [16, 17]. So far, this technology has also been applied to the detection of biomarkers. For example, Zhao et al. constructed a SERS sensor consisting of silica-coated Ag SERS nanotags and magnetic capture substrates of Fe₃O₄ microspheres to detect the content of matrix metalloproteinase 9 (MMP-9) in the serum of patients, and the measurement results were accurate to 1.03 ng/mL [22]. Wang's team used the gold-film hemisphere array (Au-FHA) immune

substrates and SiO₂@Ag immune probes to simultaneously detect the content of α -fetoprotein (AFP) and prostate-specific antigen (PSA) tumor-associated antigens in the serum of patients [23]. Quantitative detection of multiple cancer biomarkers in serum can be achieved by SERS, which is helpful for the accurate diagnosis of cervical cancer.

In the application of SERS technology, nanomaterials are not only used as immunotags and carriers of immunosubstrate [22–24] but also enhance SERS signal due to their special shape [25–27]. When the laser is incident on the tips and protrusions of nanomaterials, the free electrons on the surface and around will oscillate collectively, the local surface plasmon resonance (LSPR) effect is formed near the tips and protrusions of nanomaterials, and the local electromagnetic field is greatly enhanced, which enlarges the Raman signal [17, 28]. These tips and protrusions form a “hot spot” in SERS technology. Therefore, compared with nanoparticles with smooth and uniform morphology, nanomaterials with special tips and multiple branch angles have stronger SERS signal enhancement effect [17, 28–30]. The invisible electromagnetic field can be visualized by finite difference time domain (FDTD) simulation, and the distribution and enhancement of the electromagnetic field around the nanomaterial can be observed by simulating the laser irradiation on the surface of the nanomaterial; the SERS signal enhancement performance of nanomaterials with special morphology can be verified [31]. The Au-Ag nanoshuttles (Au-AgNSs) have arrow-shaped tip structures at both ends, which are conducive to the formation of “hot spot.” Compared with other nanomaterials, its special gold-silver alloy structure has better stability and stronger SERS activity [32]. The surface of Au nanoflowers (AuNFs) is rough, and there are many branch structures. These protrusions and branch angles are a good place to form a “hot spot” effect. AuNFs have good biocompatibility, low synthesis cost, and mild reaction conditions [33]. As a result, both Au-AgNSs and AuNFs are potential candidate for SERS detection. Compared with isolated particles, the electromagnetic field coupling of aggregated nanoparticles is stronger [34]. Assembling the nanomaterial into substrates obtains high-density “hot spot” and significant SERS signal enhancement effects [28, 29].

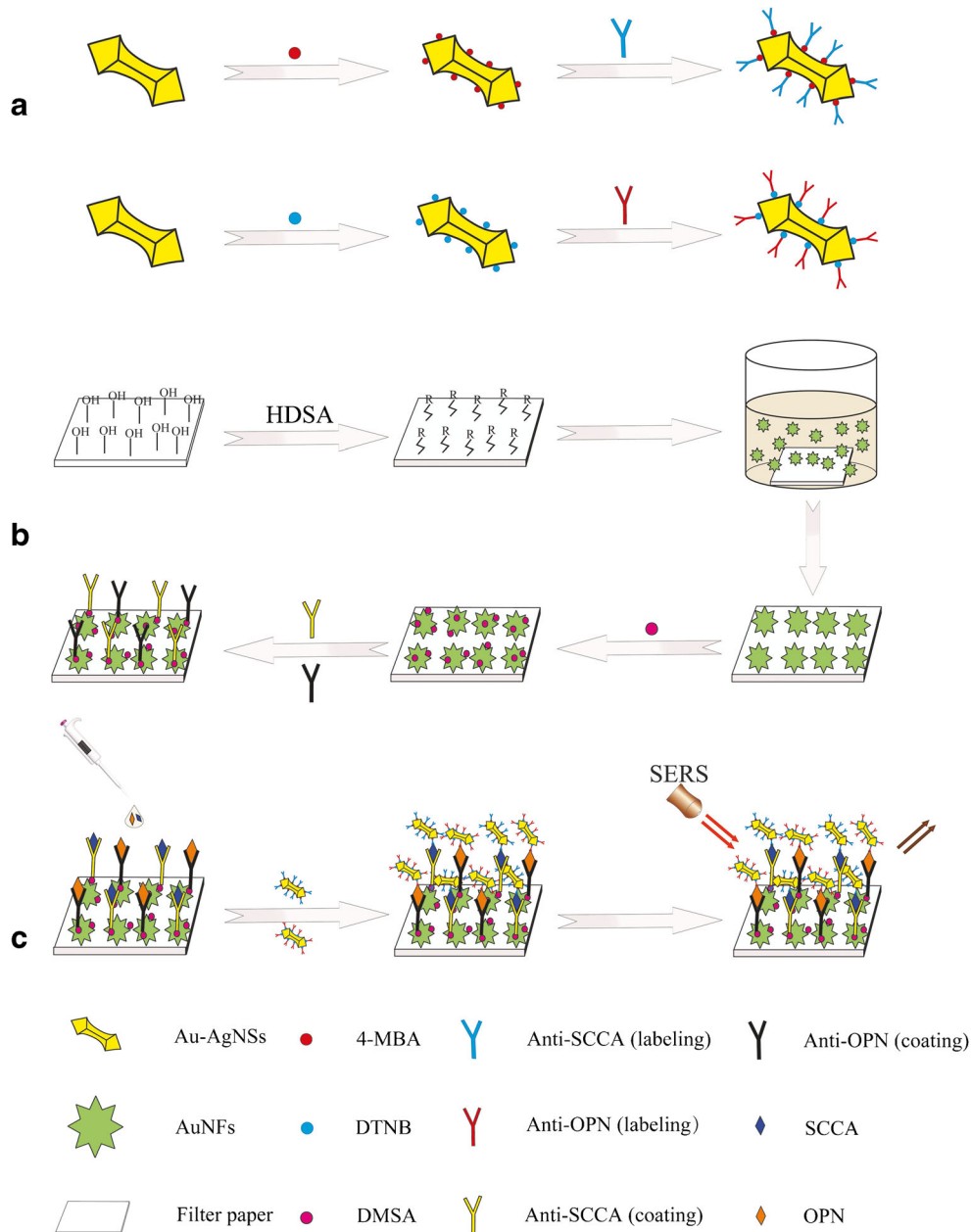
Traditional SERS substrates with different materials, such as glass or silicon wafers, are assembled with nanomaterials with different morphologies, which is not only tedious in operation but also relatively expensive [17, 35]. Paper-based SERS substrates, which are cheap, simple to fabricate, portable, and environmentally friendly, have attracted the attention of researchers [36–38]. However, the hydrophilic of the paper makes it difficult to retain the sample solution for a long time and the accuracy and sensitivity of the detection are reduced because the solution is quickly absorbed and distributed unevenly [39]. Here, we proposed a new and rapid filter paper surface modification technology; the filter paper was treated

with hexadecenyl succinic anhydride (HDSA) so that long-chain alkenyl groups replaced the hydroxyl groups on the surface of the filter paper to obtain a hydrophobic filter paper (h-paper). HDSA-treated filter paper improved the homogeneity and repeatability of the substrate by preventing the analytes and nanoparticles from being absorbed quickly and allowing it to react adequately with the substrate [40–42].

In this paper, we introduced an ultrasensitive, inexpensive, and easy to manufacture SERS-based immunoassay platform consisting of Au-AgNS tags and AuNF capture substrates based on hydrophobic filter paper for the simultaneous detection of SCCA and OPN contents in clinical serum. Illustration of SERS-based immunoassay for SCCA and OPN detection

was shown in Fig. 1. During the preparation of two SERS tags, 4-mercaptobenzoic acid (4-MBA) and 5,5'-dithiobis-(2-nitrobenzoic acid) (DTNB) were used as Raman signal molecules and conjugates for attaching antibodies (labeling) to Au-AgNSs. 4-MBA or DTNB grasped Au-AgNSs by -SH and conjugated with antibodies (labeling) by forming amide bonds with carboxyl groups. Then, h-paper-based substrates were obtained by assembling AuNFs onto HDSA-treated filter paper; next, the antibodies (coating) were coupled to obtain the capture substrates. Finally, a sandwich immunocomplex composed of SERS tags, antigen, and capture substrates were formed to quantitatively detect dual cervical cancer biomarkers. The selectivity and reproducibility of the constructed

Fig. 1 Schematic diagram (a) fabrication processes of two SERS tags (4-MBA-labeled and anti-SCCA-coupled Au-AgNSs, DTNB-labeled and anti-ONP-coupled Au-AgNSs) and (b) hexadecenyl succinic anhydride (HDSA)-treated filter paper-based AuNF capture substrate (DMSA-labeled and anti-SCCA/anti-ONP-coupled AuNFs). (c) Simultaneous detection of squamous cell carcinoma antigen (SCCA) and osteopontin (OPN) by SERS-based immunoassay platform



immunoassay platforms were evaluated, and the sensitivity was verified using the calibration curves established by SERS intensities at different antigen concentrations in PBS buffer and human serum. In addition, the SCCA and OPN in clinical serum collected from healthy subjects; cervical intraepithelial neoplasia I (CINI), CINII, and CINIII; and cervical cancer patients were analyzed by the proposed immunoassay proposal. The results of SERS were in good agreement with those of ELISA, which indicated the potential of SERS-based immunoassay for early clinical diagnosis of cervical cancer.

Materials and methods

Materials

All reagents can be used directly without further purification. Chloroauric acid tetrahydrate (HAuCl_4), silver nitrate (AgNO_3), sodium borohydride (NaBH_4), sodium oleate, hydrochloric acid (HCl), ascorbic acid (AA), glycine ($\text{C}_2\text{H}_5\text{NO}_2$), absolute ethanol, dopamine hydrochloride, sodium hydroxide (NaOH), hexadecyl trimethyl ammonium bromide (CTAB), hexadecyl succinic anhydride (HDSA), filter paper, and all the above materials were obtained from Yangzhou Feichang Chemicals Co. Ltd. (China). 4-Mercaptobenzoic acid (4-MBA), 5,5'-dithiobis-(2-nitrobenzoic acid) (DTNB), dimercaptosuccinic acid (DMSA), N-hydroxysuccinimide (NHS), and 1-ethyl-3-(3-dimethylaminopropyl) carbodiimide (EDC) were obtained from Yangzhou Noah Chemical Co. Ltd. (China). SCCA, OPN, anti-SCCA antibodies, anti-OPN antibodies, and ELISA kits were bought from Shanghai Sangon Biotech (China). In all experiments, the water was used directly from Milli-Q (resistivity $> 18 \text{ M } \Omega \text{ cm}$, Millipore, USA) without any modification.

Collection and processing of blood samples

We collected a total of 150 blood samples from the College of Clinical Medicine of Yangzhou University, including 30 healthy subjects, 30 CINI, 30 CINII, 30 CINIII, and 30 cervical cancer patients. Table 1 displayed the details information of the volunteers. Five milliliter venous blood was drawn

before breakfast for each volunteer. After centrifugation (3000 rpm, 10 min, $4 \text{ }^\circ\text{C}$), the serums were stored at $-80 \text{ }^\circ\text{C}$ for subsequent detection. During the experiment, the ethical guidelines issued by the Council for International Organizations of Medical Sciences were strictly followed and informed consent was signed with volunteers. This study was approved by the Ethics Committee of the College of Clinical Medicine of Yangzhou University and followed the guidelines of the Declaration of Helsinki.

Synthesis of Au-AgNSs

The synthesis of Au-AgNSs was divided into four steps. Firstly, 0.1 mL HAuCl_4 (25 mM) and 9.9 mL CTAB (0.1 M) were added into the 0.6 mL ice-cold NaBH_4 (10 mM) solution, under stirring (700 rpm) for 2 min. To synthesize gold seeds, the solution was placed in a water bath at $30 \text{ }^\circ\text{C}$ for 2 h. Secondly, 1.44 mL AgNO_3 (10 mM) and 2 mL HAuCl_4 (25 mM) were injected into 100 mL mixed solution containing CTAB (0.037 M) and sodium oleate (0.078 M), and the result solution was stirred (700 rpm) at $30 \text{ }^\circ\text{C}$ for 90 min. After that, 0.42 mL HCl (37%) and 0.16 mL AA (0.1 M) were added successively and stirred for 5 min respectively. It was followed by injecting 0.08 mL gold seeds, and stirred gently at $30 \text{ }^\circ\text{C}$ for 10 h. The solution was centrifuged twice (10,000 rpm, 15 min) before further use. Thirdly, 0.182 g CTAB and 5 mL of solution in the second step were added into a 25-mL beaker and stirred evenly. Then, 5 mL glycine acid (0.2 M), 30 μL NaOH (2 M), 40 μL HAuCl_4 (25 mM), and 0.2 mL AgNO_3 (10 mM) were added under vigorous stirring at $27 \text{ }^\circ\text{C}$. Finally, 0.2 mL AA (0.1 M) was added and stirred for 30 s, then the synthesis of Au-AgNSs was finished after being aged for 1 h, at which point, the sample was washed once by centrifugation (7500 rpm, 10 min) and store at $4 \text{ }^\circ\text{C}$.

Preparation of SCCA SERS tags and OPN SERS tags

Firstly, 200 μL 4-MBA (1 mM, in ethanol) was added into 5 mL of Au-AgNS solution, and then shaken for 1 h at room temperature. After centrifugation (7000 rpm, 5 min), the supernatant was discarded and dispersed into 5 mL PBS. Secondly, 50 μL EDC (150 mM) and 50 μL NHS (30 mM) were added to the solution in sequence. After shaking for

Table 1 Information of the volunteers in this study

Group		Healthy subjects	CINI	CINII	CINIII	Cervical cancer
Age (years)	Minimum	22	26	34	39	39
	Median	27	37	42	48	55
	Maximum	33	46	53	59	62
Sample number		30	30	30	30	30

1.5 h, the carboxyl groups (-COOH) were activated and ready to connect the antibodies (labeling). Next, 50 μL anti-SCCA (labeling) (200 $\mu\text{g}/\text{mL}$) was added before the solution was incubated at 37 $^{\circ}\text{C}$. After 2 h, the SCCA SERS tags were successfully synthesized. The synthesis processes of OPN SERS tags were the same as that of SCCA SERS tags. During the synthesis processes of OPN SERS tags, the Raman signal molecule was DTNB and the antibody was anti-OPN (labeling).

Synthesis of AuNFs

AuNFs was synthesized by one-step synthesis method [33]. Briefly, 1.6 mL HAuCl_4 (25 mM) was added into a 100-mL beaker followed by adding 20 mL of ultrapure water. The solution was placed in a magnetically stirred water bath and heated to 60 $^{\circ}\text{C}$ with vigorous stirring. At this time, 4 mL dopamine hydrochloride solution (53 mM) was added and kept stirring at 60 $^{\circ}\text{C}$ for 30 min to generate AuNFs.

Preparation of capturing substrates

The 10% hexanol HDSA solution was evenly sprayed on the surface of the filter papers and placed in an oven at 100 $^{\circ}\text{C}$ for 10 min to obtain h-papers. The h-papers were cut into square pieces of 80 mm \times 80 mm size, and then directly immersed in the solution of AuNFs for 12 h; the electrostatic interaction between the AuNFs and a large number of long-chain alkenyl groups allowed the AuNFs to firmly adsorb on the h-paper. At the same time, the filter paper contained some holes, and capillarity also promoted the adsorption of AuNFs on it. Those AuNFs that did not adsorb tightly were washed away with water (three times) and dried at room temperature to obtain AuNF substrates. In the following steps, the anti-SCCA (coating) and anti-OPN (coating) were modified onto the AuNFs which adsorbed on the h-papers to prepare capturing substrates. The AuNF substrates were soaked with 5 mL of DMSA solution and washed twice with water after 2 h of reaction. Then, the DMSA-modified AuNF substrates were soaked with 5 mL of the mixed solution of EDC (150 mM) and NHS (30 mM) for 30 min to activate the carboxyl groups (-COOH) of DMSA. Ten microliter of 200 $\mu\text{g}/\text{mL}$ anti-SCCA (coating) and 200 $\mu\text{g}/\text{mL}$ anti-OPN (coating) mixture were added to the surface of functionalized AuNF substrates and then incubated at 37 $^{\circ}\text{C}$. After 4 h, the antibody connection was completed and then the substrates were washed twice with PBS before naturally drying. At this point, the fabrication of SCCA and OPN capturing substrates were completed.

Simultaneous detection

The detection process of SCCA and OPN was as follows: First, 20 μL of the antigen solution containing SCCA and

OPN was added onto the prepared capturing substrates and kept at 37 $^{\circ}\text{C}$ for 1 h. Then, the mixed solution of SCCA SERS tags (10 μL) and OPN SERS tags (10 μL) was dripped. After reaction about 1 h at 37 $^{\circ}\text{C}$, the excess reactants were washed away by using PBS buffer (three times) before SERS measurements [6, 8].

Characterization

After the nanomaterials were synthesized, UV-visible spectra were acquired with an UV/Vis/NIR spectrophotometer (Cary UV-5000, Agilent, America). The morphology of nanomaterials was characterized by transmission electron microscopy (TEM) (Tecnai 12, Philips, Netherlands) and field emission scanning electron microscopy (FESEM) (S-4800 II, Hitachi, Japan). Selected area electron diffraction (SAED) images and high-resolution TEM (HRTEM) of nanomaterials were obtained from S-twin TEM (Tecnai G2 F30, FEI, America). Microscopic infrared spectrometer (Cary 610/670, Varian, America) was used to measure Fourier transform infrared spectroscopy (FT-IR). SERS spectra of all samples were measured by using Renishaw inVia microRaman in the 600–1800 cm^{-1} range at room temperature. And SERS scans (excitation wavelength 785 nm, objective 50 \times , laser power 5 mW, acquisition time 10 s) were performed on five sites for each sample and the average SERS spectra were taken.

Simulation of electromagnetic field distribution and extinction spectrum

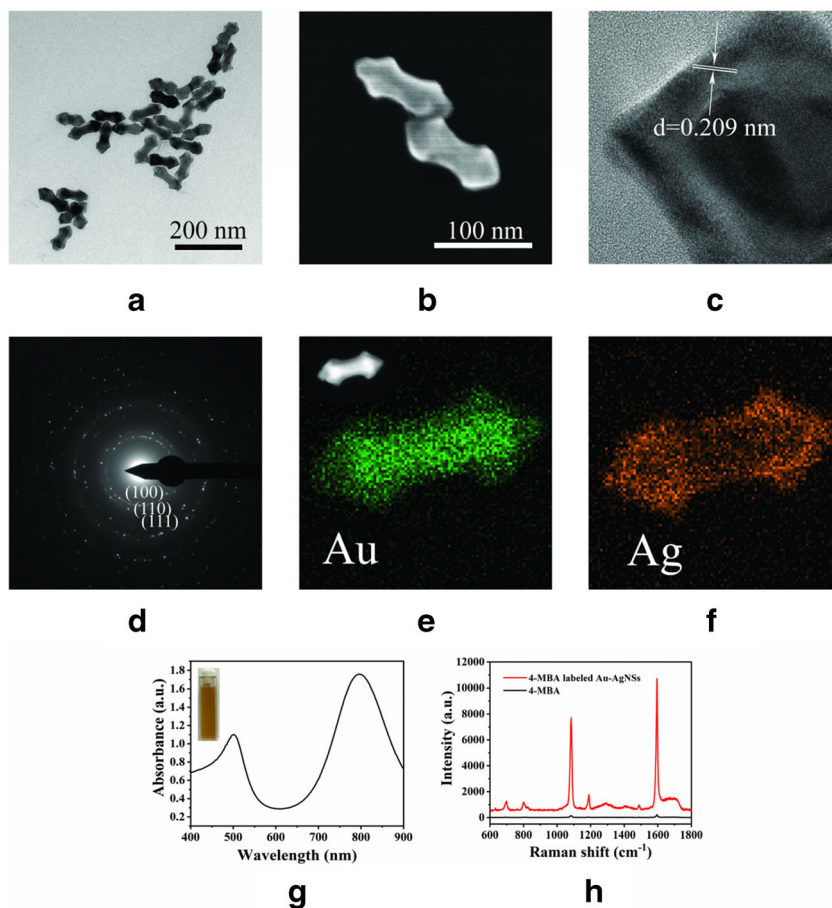
In order to understand the enhancement of the electromagnetic field of AuNFs, FDTD simulation was performed using the 8.9 version software provided by Lumerical Solutions Inc. The electromagnetic field distribution and enhancement of monomer and dimer AuNFs excited by incident light with a wavelength of 785 nm were simulated. The simulation used the TEM images of monomer and dimer AuNFs. The SERS-based immunoassay platforms would be tested in air at room temperature, so its background was set to 1. The perfect matching layer was applied to truncate the simulation domain in the x, y, and z axis directions [43]. In addition, the extinction spectra of single AuNF and AuNF dimer were calculated, and the wavelength range of the light source was 400–900 nm. The AuNFs were dispersed in water at room temperature, and the background was set to 1.33.

Results and discussion

Characterization of Au-AgNSs

TEM images and SEM images were used to characterize the morphology and structure of Au-AgNSs. Figure 2a shows that

Fig. 2 **a** TEM images, **b** SEM images, and **c** HRTEM image of Au-AgNSs. **d** SAED pattern of Au-AgNSs. **e** Au and **f** Ag elemental mapping of Au-AgNS. **g** UV-visible spectrum of Au-AgNSs. **h** Raman spectra of 4-MBA-labeled Au-AgNSs and 4-MBA



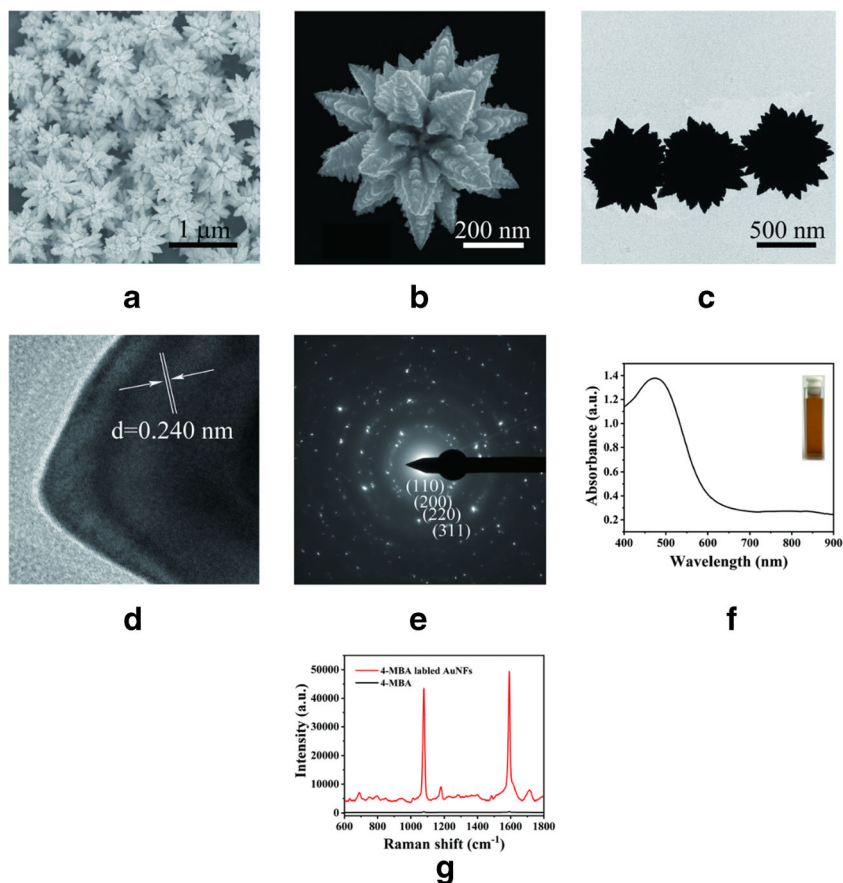
a large number of Au-AgNSs with complete structure and uniform morphology were prepared. All of them have sharp tips at each end, like a double-headed arrow. Figure 2b was a high magnification image of Au-AgNSs from SEM to further observe its morphology. The length of the Au-AgNSs was about 120 nm with the width of 30 nm. Figure 2c showed the HRTEM image; the tip lattice spacing was 0.209 nm, which corresponded to the Au {100} plane. To further understand its growth, SAED image in Fig. 2d was taken, with corresponding {100}, {110}, and {111} planes [44]. Compared with the {110} plane, Ag atoms preferred to grow on the {100} and {111} plane, thus forming a special arrow structure. Figure 2e and f display the distribution of Au and Ag elements, and it can be seen that Au-AgNS was not a simple Ag-coated Au or Au-coated Ag structure. This Au-Ag alloy structure had better thermodynamic stability [32]. It further verified the synthesis of Au-AgNSs. In order to further understand the morphological characteristics of the Au-AgNSs, the UV-visible spectrum was measured as shown in Fig. 2g. Because of its shuttle structure, there were two characteristic absorption peaks, namely a transverse absorption peak (501 nm) and a lateral absorption peak (797 nm) [32]. Figure 2h displays the Raman spectra of 4-MBA-labeled Au-AgNSs and 4-MBA. Due to the two SERS characteristic

peaks at 1080 cm^{-1} and 1593 cm^{-1} , 4-MBA was selected as the Raman signal molecule. The Raman signal of 4-MBA molecules was almost negligible. When 4-MBA was labeled on Au-AgNS, the Raman signal was greatly enhanced. It might be that the two tips of Au-AgNSs act as “hot spots,” leading to the enhancement effect [44]. As a result, it can be used as a good material for the preparation of SERS tags.

Characterization of AuNFs

The overall morphology, structure, and lattice of the AuNFs were characterized by SEM and TEM. The low magnification SEM image in Fig. 3a showed that AuNFs with multiple branching structures and good dispersibility were prepared in large quantities, which laid the foundation for assembling the substrates [33, 35]. The high magnification SEM image in Fig. 3b showed the details of the AuNF, such as a blooming flower composed of multiple petals. There were many secondary triangular bulges on each petal extending in their own specific directions. These tips and bulges facilitate the formation of “hot spots” [28]. It could be predicted that the AuNFs prepared had a good SERS enhancement effect [17]. The multiple branching structures of AuNFs were further indicated by the TEM image Fig. 3c, and its particle size was about

Fig. 3 **a** SEM images of AuNFs. **b** High magnification SEM image of AuNF. **c** TEM images and **d** HRTEM image of AuNFs. **e** SAED pattern and **f** UV-visible spectrum of AuNFs. **g** Raman spectra of 4-MBA-labeled AuNFs and 4-MBA



600 nm. HRTEM image in Fig. 3d presented the lattice conditions of the branch angle of the AuNF, with a lattice spacing of 0.240 nm. The crystal structure of AuNFs could be understood by the SAED image. As shown in Fig. 3e, the four rings correspond to $\{110\}$, $\{200\}$, $\{220\}$, and $\{311\}$ planes, which proved that the AuNF was pure gold nanostructure with good crystallization [33]. From the UV-visible spectrum of Fig. 3f, the absorption peak of AuNFs was at 473 nm. SERS signal enhancement performance of AuNFs was verified by labeling 4-MBA. As shown in Fig. 3g, 4-MBA-labeled AuNFs had a very strong Raman spectral signal, which may benefit from many “hot spots” of AuNFs [28].

FDTD simulation

In order to understand the influence of structural parameters of AuNFs on SERS enhancement, distributions of electromagnetic field of single AuNF and AuNF dimer were investigated by FDTD method. Figure 4a presents the electric field distribution for single AuNF after excitation by incident light with a wavelength of 785 nm. As expected, its sharp branch angle had a strong electromagnetic field enhancement effect, and the electromagnetic field was also enhanced in the region among branches. Figure 4b shows the enhancement of the electromagnetic field of AuNF dimer and the enhancement of the

electromagnetic field of the edge-distributed branches was not significantly different from that of single AuNF. However, the maximum electromagnetic field enhancement is located in the nanogap junction for AuNF dimer [28]. This result was attributed to the coupling effect of the electromagnetic field between the AuNFs, which could greatly increase the number of “hot spots” for SERS measurement [43, 45, 46]. As shown in the Electronic Supplementary Material (ESM) Fig. S2, the extinction spectra of single AuNF and AuNF dimer in water were calculated by FDTD simulation, and the wavelength ranges from 400 to 900 nm. The comparison between the experimental spectrum (Fig. 3f) and the simulated spectra (ESM Fig. S2) showed that the change trend of the absorption peak position in the spectra was consistent. There was only a slight difference in their peak positions (473 nm and 478 nm), which was due to the fact that the experimental spectrum was the superposition of the absorption spectra of many AuNFs with certain differences in morphological sizes. In conclusion, these results demonstrated the accuracy of the simulation results.

Characterization of AuNF substrates

The substrate preparation condition was optimized by comparing SERS mapping recorded on the paper-based AuNF

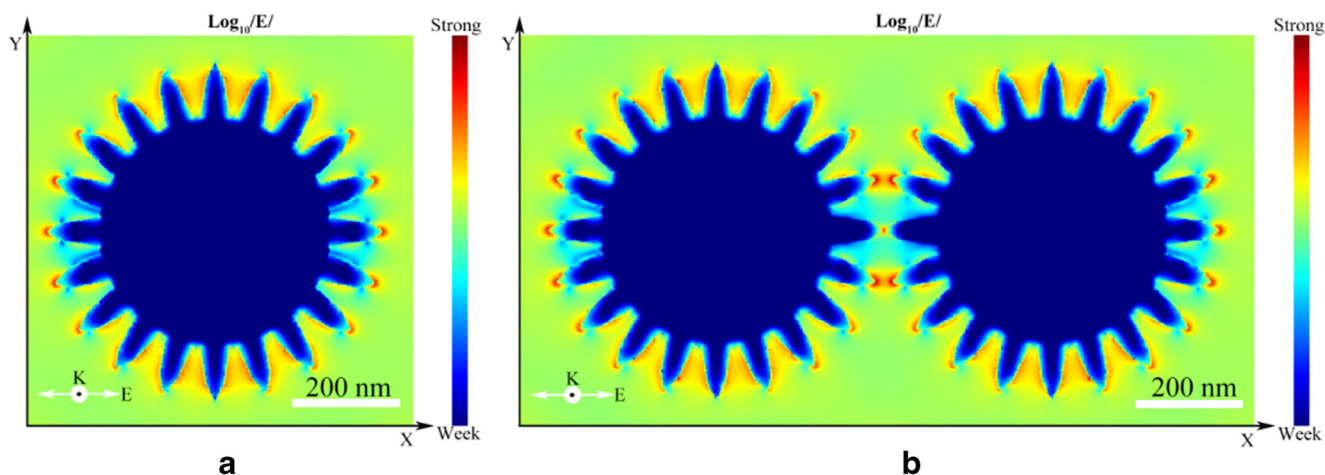


Fig. 4 FDTD simulation of electric field distribution of (a) single AuNF and (b) AuNF dimer

substrates and h-paper-based AuNF substrates. The two prepared substrates were labeled with 4-MBA (1×10^{-4} M) to verify their uniformity and enhancement effect of SERS signal. Figure 5a and d showed the SERS mapping of paper-based AuNF substrates and h-paper-based AuNF substrates, respectively. The scanning range on the substrate was 50×50 mm and the intensity of SERS peak at 1593 cm^{-1} was plotted at each grid point. The intensity distribution of SERS signal on the substrate was understood according to the

change of color matching scheme from blue (lowest) to red (highest). As shown in Fig. 5a, the color distribution was irregular, indicating that the homogeneity of paper-based AuNF substrate was poor. Figure 5d shows that the color of SERS mapping were basically the same, which indicated that h-paper-based AuNF substrate had a very uniform SERS enhancement effect. Then, we randomly selected five different spots on two substrates and measured their SERS spectra. Figure 5b and c illustrate the deviation of the signal intensities

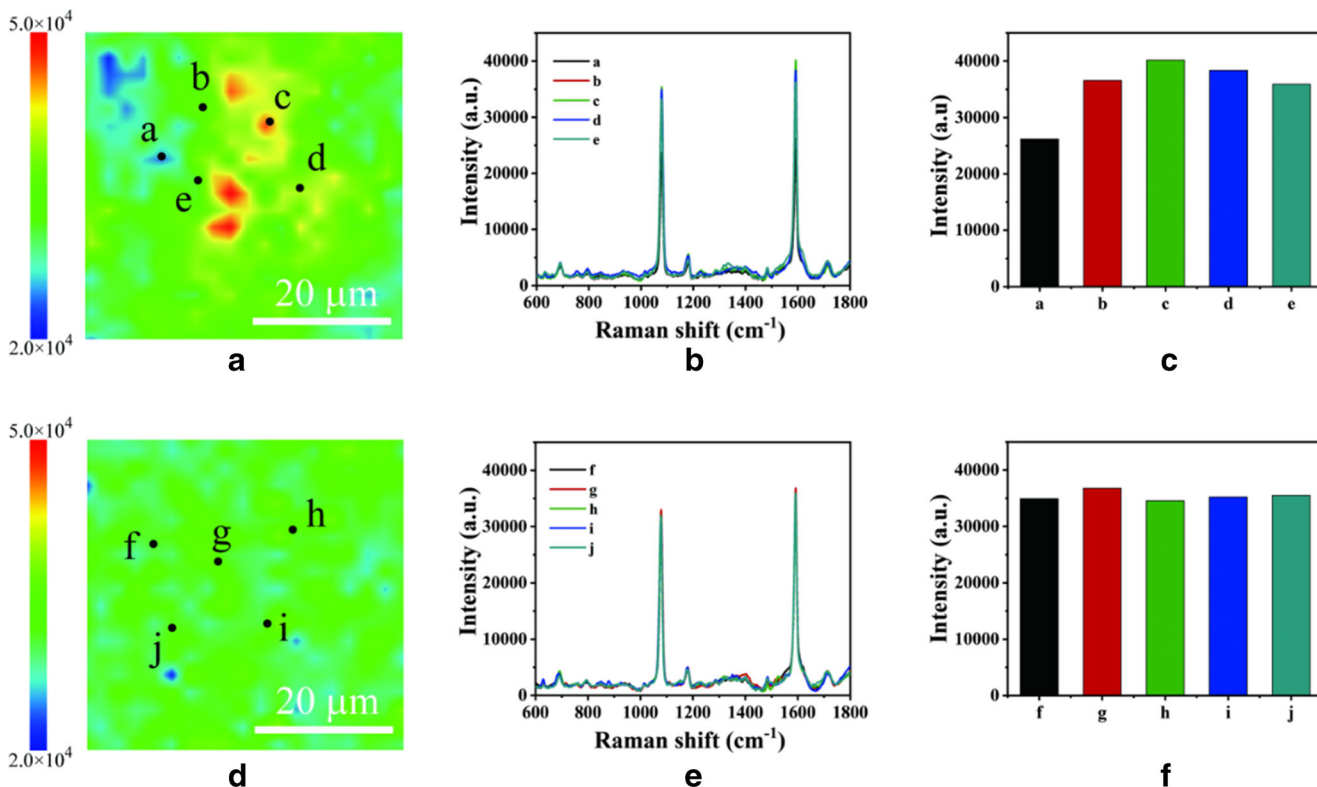


Fig. 5 a SERS mapping for 4-MBA on paper-based AuNF substrate. b SERS spectra of a, b, c, d, and e were randomly selected on the paper-based AuNF substrate. c Intensity bar graphs of characteristic peaks at 1593 cm^{-1} for a, b, c, d, and e. d SERS mapping for 4-MBA on h-paper-

based AuNF substrate. e The SERS spectra of f, g, h, i, and j were randomly selected on the h-paper-based AuNF substrate. f Intensity bar graphs of characteristic peaks at 1593 cm^{-1} for f, g, h, i, and j

at 1593 cm^{-1} for the five points on the paper-based AuNF substrate was 34.81%. At the same time, Fig. 5e and f revealed the deviation of the signal intensities at 1593 cm^{-1} for the five points on the h-paper-based AuNF substrate was only 5.96%. This result further demonstrated that the h-paper-based AuNF substrate had better homogeneity [38]. The hydrophobic reagent changed the filter paper from hydrophilic to hydrophobic, and the samples were more evenly distributed on the AuNF substrate, which improved the homogeneity of the substrate [39, 40]. In order to understand the SERS enhancement capability of h-paper-based AuNF substrates, the SERS enhancement factor (EF) was calculated by referring to the following equation $EF = (I_{\text{SERS}}/C_{\text{SERS}})/(I_{\text{RS}}/C_{\text{RS}})$, where I represented the intensity of the peak at 1593 cm^{-1} and C represented the concentration of the analyte, SERS and RS denoted SERS conditions and non-SERS conditions [23, 25, 28]. Finally, when $C_{\text{SERS}} = 1 \times 10^{-4}\text{ M}$ and $C_{\text{RS}} = 1 \times 10^0\text{ M}$, the corresponding spectra were shown in ESM Fig. S1; EF value was obtained to be 5.58×10^5 .

The distribution of AuNFs on the h-paper could be observed by SEM image in Fig. 6a. A large number of AuNFs with uniform morphology were assembled on the h-paper. Figure 6b shows the average SERS spectra of AuNF substrates labeled with 4-MBA after being stored for 1 day, 5 days, 10 days, and 15 days. The peak and shape of these SERS spectra did not change, but the signal intensity decreased slightly. As illustrated in Fig. 6c, the intensity of SERS peak at 1593 cm^{-1} decreased by 7.79% after 15 days of storage, indicating that the SERS enhancement effect of the substrate was stable. All the above experiments proved that the prepared AuNF substrate had good homogeneity and stability [17].

FT-IR characterization of SERS tags and capturing substrate

The preparation processes of two SERS tags and AuNF capturing substrates were characterized by FT-IR. The unreacted

EDC and NHS were washed away to avoid interference with the results. ESM Fig. S3a showed that the pure Au-AgNSs had no obvious infrared (IR) peaks. After being labeled with the SERS signal molecules (4-MBA), a prominent peak in FT-IR spectrum appeared at 1679 cm^{-1} in ESM Fig. S3b, which belonged to the C=O amide I stretching from the carboxyl groups of 4-MBA [47]. FT-IR spectrum of anti-SCCA-conjugated Au-AgNS tags was shown in ESM Fig. S3c; the IR peak at 1631 cm^{-1} corresponded to C=O amide I stretching, the IR peak at 1560 cm^{-1} belonged to the N-H amide II stretching, and the IR peak at 1267 cm^{-1} belonged to C-N stretching [48]. It was indicated in ESM Fig. S3d that the Au-AgNSs were labeled with DTNB; the IR peak at 1645 cm^{-1} was associated with C=O stretching vibration of DTNB. ESM Fig. S3e showed FT-IR spectrum of the anti-OPN-conjugated Au-AgNSs tags. The peaks at 1642 cm^{-1} , 1565 cm^{-1} , and 1222 cm^{-1} were assigned to C=O stretching, N-H stretching, and vibration peak of C-N, respectively [49]. ESM Fig. S3f showed the FT-IR spectrum of AuNFs; no IR peaks appeared. In ESM Fig. S3g, after coupled with DMSA, the IR peak appearing at 1701 cm^{-1} corresponded to the C=O stretching vibration peak of amide I. As shown in ESM Fig. S3h, the IR peaks at 1637 cm^{-1} , 1525 cm^{-1} , and 1224 cm^{-1} corresponded to the stretching vibration peaks of C=O, N-H, and C-N, respectively [49, 50]. It was indicated that the formation of amide bonds and the antibodies were successfully modified on AuNF substrate. In summary, the two SERS tags and AuNF capturing substrates were successfully prepared.

Selectivity and repeatability of SERS-based immunoassay platform

According to the SERS-based immunoassay protocol, SCCA and OPN could be quantitatively analyzed by the SERS signal of 4-MBA and DTNB. To verify its selectivity, SERS spectra of blank sample and different protein samples (CA125, CEA, SCCA, OPN) with the same concentration were detected in

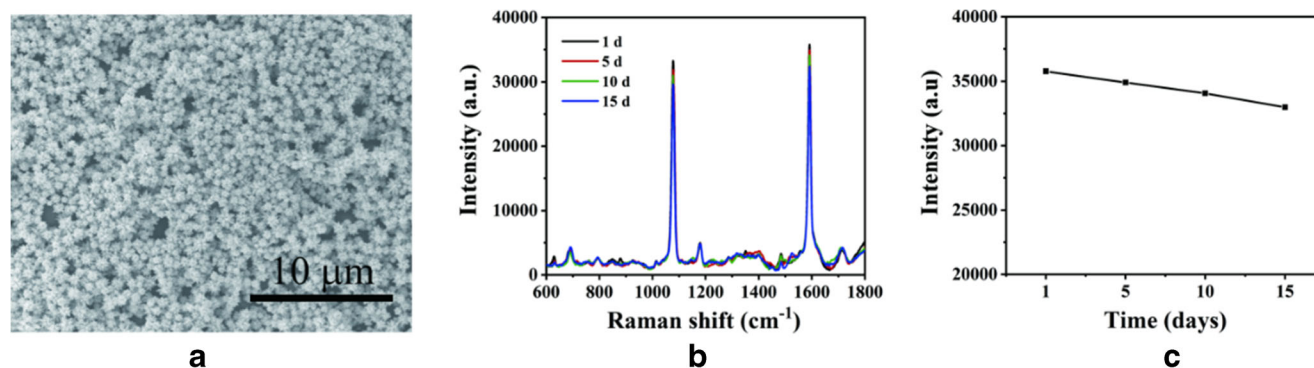


Fig. 6 **a** SEM image of the AuNF substrate, with its digital photo in the upper left corner. **b** The average SERS spectra of AuNF substrates labeled with 4-MBA after being stored for 1 day, 5 days, 10 days, and

15 days. **c** The line chart corresponded to the intensities of SERS peaks at 1593 cm^{-1} of the SERS spectra

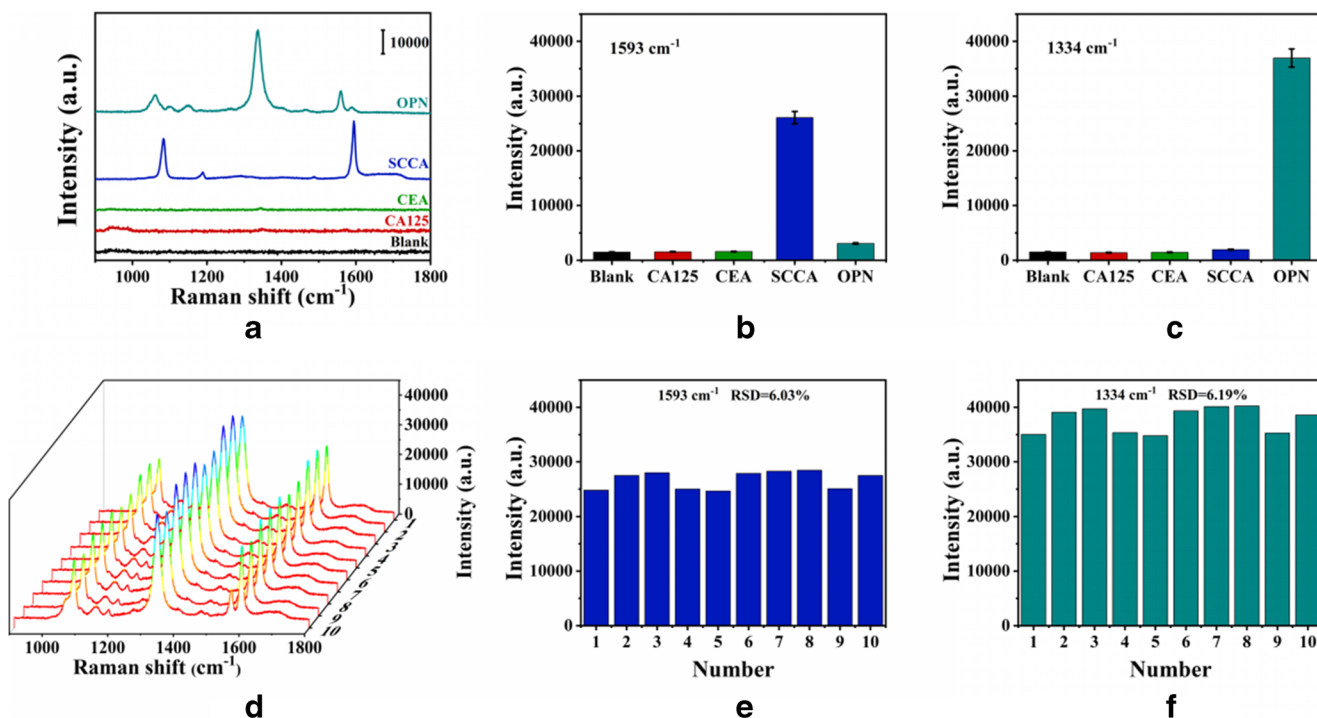


Fig. 7 SERS spectra of (a) blank sample and different protein samples, and the corresponding SERS intensities at (b) 1593 cm^{-1} and (c) 1334 cm^{-1} . (d) The repeatability of SERS-based immunoassay platforms. The corresponding intensities of SERS peaks at (e) 1593 cm^{-1} and (f) 1334 cm^{-1}

Fig. 7a. The strong SERS signal was observed when the sample contained SCCA or OPN, and there was no obvious SERS signal in other samples. This was due to the fact that other samples could not form sandwich immunocomplexes during detection. Figure 7b and c were bar graphs of the SERS intensities of each sample at 1593 cm^{-1} and 1334 cm^{-1} . The SERS intensities of the sample containing SCCA or OPN were much higher than that of the other samples, and the two characteristic peaks were convenient to distinguish. The results showed that the constructed SERS-based immunoassay platform had good selectivity for SCCA and OPN. Furthermore, the repeatability of this method was verified. Ten different batches of SERS-based immunoassay platforms were prepared for detection of the same human serum sample containing SCCA ($10\text{ }\mu\text{g/mL}$) and OPN ($10\text{ }\mu\text{g/mL}$). As shown in Fig. 7d, there were no significant difference among these SERS spectra. Figure 7e and f show the SERS intensities of different batch platform at 1593 cm^{-1} and 1334 cm^{-1} . The relative standard deviations (RSD) were 6.03% (1593 cm^{-1}) and 6.19% (1334 cm^{-1}), which indicated that the designed SERS-based immunoassay platforms had good repeatability.

Simultaneous detection of SCCA and OPN in PBS and human serum

The calibration curve and the detection limits of the immunoassay were studied by simultaneously detecting the same final concentration of SCCA and OPN solutions from 10 pg/mL to

$10\text{ }\mu\text{g/mL}$, which was obtained by dissolving SCCA and OPN in PBS buffer. Figure 8a shows that the SERS signal continuously weakened when the concentration of SCCA and OPN decreased, which was due to the formation of immunocomplexes decreasing. A good linear relationship was found between the logarithm of SCCA concentration and SERS intensities at 1593 cm^{-1} as shown in Fig. 8b. The linear regression equation was $y = 3664.024x - 1101.758$, the correlation coefficient (R^2) was 0.975, the peak intensity at 1593 cm^{-1} was represented by y , and x was the logarithm of the SCCA concentration. Figure 8c shows the linear relationship between the logarithm of OPN concentration (x) and the SERS intensities (y) at 1334 cm^{-1} with the linear equation $y = 5186.647x - 1497.099$, $R^2 = 0.982$. Finally, the lowest concentration was defined as the signal that could produce three times the standard deviation stronger than the blank control [51], and the detection limits of SCCA and OPN in PBS were calculated according to their linear equations, which were 6.371 pg/mL and 4.118 pg/mL , respectively.

The composition of human serum was more complicated than that of PBS solution. The ability of the immunoassay platform to analyze clinical serum was verified by detecting the same final concentration of SCCA and OPN serum samples from 10 pg/mL to $10\text{ }\mu\text{g/mL}$, which were prepared by diluting SCCA and OPN dissolved in blank human serum. A blank control was obtained by analyzing blank human serum samples. Figure 8d displayed the concentration-dependent SERS spectra, and the SERS intensities at 1593 cm^{-1} and

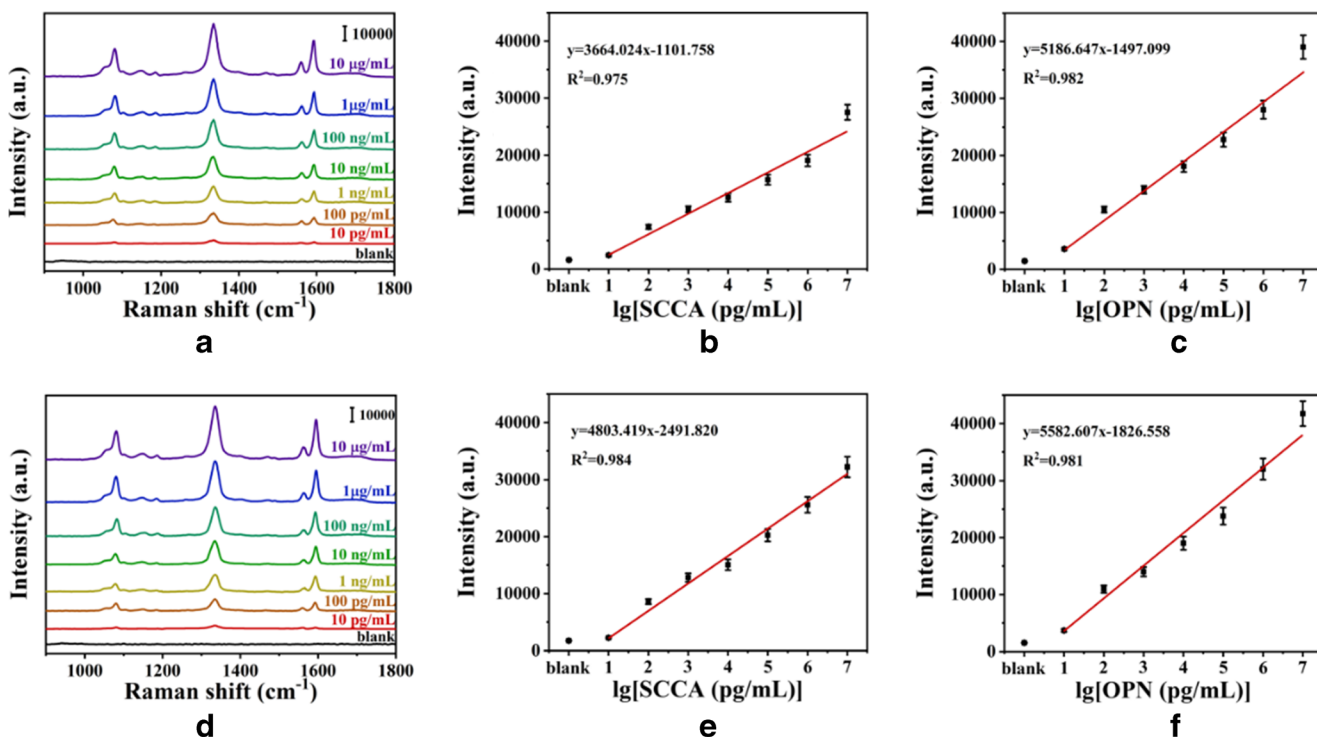


Fig. 8 Average SERS spectra of five independent measurements of (a) antigen concentration gradient in PBS buffer, (b) and (c) the linear relationship between the intensities of SERS peaks at 1593 cm^{-1} (1334 cm^{-1}) and the logarithm of SCCA (OPN) concentration. Average

SERS spectra of five independent measurements of (d) antigen concentration gradient in blank human serum, (e) and (f) the linear relationship between the intensities of SERS peaks at 1593 cm^{-1} (1334 cm^{-1}) and the logarithm of SCCA (OPN) concentration

1334 cm^{-1} decreased proportionally with the decreasing concentration of SCCA and OPN. Figure 8e and f show the linear relationships between the logarithm of the concentration of SCCA and OPN in human serum and SERS intensities (1593 cm^{-1} and 1334 cm^{-1}). The linear regression equations were $y = 4803.419x - 2491.820$ and $y = 5582.607x - 1826.558$ with the correlation coefficient $R^2 = 0.984$ and $R^2 = 0.981$. The calculated detection limits were 8.628 pg/mL for SCCA and 4.388 pg/mL for OPN in human serum, respectively. In calculating the recovery values, the contents of SCCA and OPN in blank human serum were very low, and the concentration was further reduced in the process of dilution; their effects could be ignored. ESM Table S1 showed the recovery

values of SCCA and OPN in human serum samples detected by SERS immunoassay platform. Except for the large deviation in recovery of maximum spiked concentration, the recovery percentages of SCCA and OPN spiked serum samples range from 89.45 to 107.40%. The results confirmed the ability of SRES immunoassay platform to detect SCCA and OPN in human serum.

Clinical application

The feasibility of SERS-based immunoassay platform in clinical application was further validated by detecting the collected 150 serum samples (healthy subjects; CIN I, CIN II, and

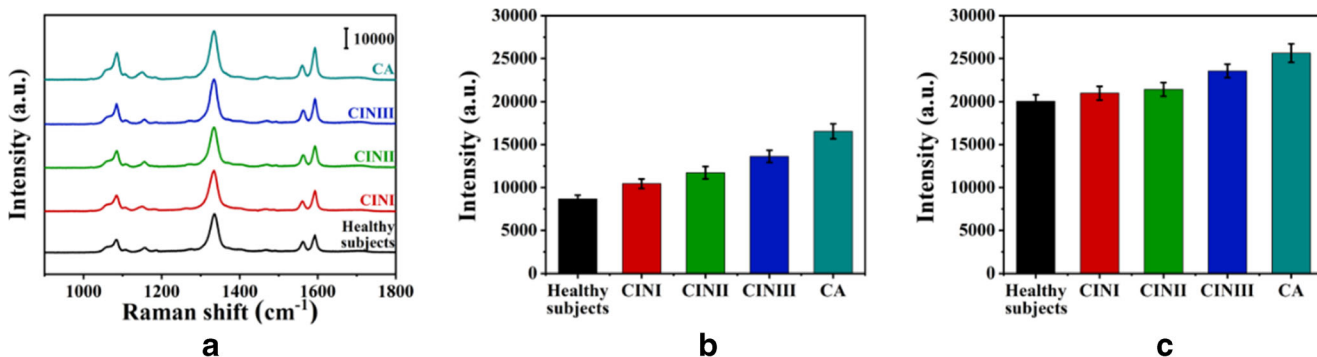


Fig. 9 a The average SERS spectra of clinical samples, and the corresponding SERS intensities at b 1593 cm^{-1} and c 1334 cm^{-1} in SERS spectra

Table 2 Detection results (average values) of clinical serum samples using SERS and ELISA method

Sample	SCCA			OPN		
	SERS (ng/mL)	ELISA (ng/mL)	Relative error (%)	SERS (ng/mL)	ELISA (ng/mL)	Relative error (%)
Healthy subject	0.210 ± 0.023	0.223	-5.83	8.279 ± 0.939	8.670	-4.51
CINI	0.493 ± 0.058	0.462	6.71	12.134 ± 1.126	11.484	5.66
CINII	0.912 ± 0.096	0.858	6.29	14.554 ± 1.518	15.256	-4.60
CINIII	2.270 ± 0.195	2.132	6.47	35.156 ± 3.834	33.254	5.72
Cervical cancer	9.204 ± 0.814	9.750	-5.60	83.176 ± 9.749	87.453	-4.89

CINIII; and cervical cancer patients) and their average SERS spectra were shown in Fig. 9a. Figure 9b and c show the intensities of SERS peaks at 1593 cm^{-1} and 1334 cm^{-1} of different samples. From the corresponding bar graphs, it could be found that the SERS intensities of the two antigens in healthy subjects were the lowest. With the development of the course of disease, the SERS intensities of the two antigens increased continuously. The linear regression equation obtained in human serum could be used to calculate the concentrations of SCCA and OPN in each sample. The results measured by the constructed SERS-based immunoassay platform were compared with those measured by ELISA method, and the specific data as displayed in Table 2. The results of the two methods were consistent, indicating that SERS could be competent for the practical application of simultaneous detection of SCCA and OPN in the serum of patients.

Conclusion

In this work, a novel and ultra-sensitive SERS-based immunoassay platform consisting of Au-AgNS tags and AuNF capture substrates based on h-paper was developed, which was used to simultaneously detect the SCCA and OPN levels in clinical samples. FDTD simulation confirmed that AuNF aggregates could generate ultra-high-density “hot spots” to effectively enhance the SERS signal. The experimental results show that the proposed immunoassay platforms not only displayed a good performance in selectivity and repeatability but also had low detection limits for SCCA and OPN in a wide dynamic range. After the filter paper was treated with HDSA, the homogeneity of the AuNF substrate was improved. Finally, SERS was successfully applied to quantify the SCCA and OPN in clinical serums of healthy subjects; CINI, CINII, and CINIII; and cervical cancer patients. Therefore, the proposed immunoassay proposal with low cost, simple operation, and high selectivity was expected to be applied in the screening for cervical cancer.

Funding information Financial support was from the National Natural Science Foundation of China (No. 81701825), the Social Development Foundation of Jiangsu (No. BE2018684), the Natural Science Foundation of the Jiangsu Higher Education Institutions of China (No.17KJB416012), Yangzhou Science and Technology Project (No.YZ2017075), and Contract for Maternal and Child Health Research Projects in Jiangsu Province (No. F201809).

Compliance with ethical standards

This study was approved by the Ethics Committee of the College of Clinical Medicine of Yangzhou University and followed the guidelines of the Declaration of Helsinki.

Conflict of interest The authors declare that they have no conflict of interest.

References

- Cohen PA, Jhingran A, Oaknin A, Denny L. Cervical cancer. *Lancet*. 2019;393:169–82.
- Koh WJ, Abu-Rustum NR, Bean S, Bradley K, Campos SM, Cho KR, et al. Cervical cancer, version 3.2019, NCCN clinical practice guidelines in oncology. *J Natl Compr Cancer Netw*. 2019;17:64–84.
- Marth C, Landoni F, Mahner S, McCormack M, Gonzalez-Martin A, Colombo N. Cervical cancer: ESMO clinical practice guidelines for diagnosis, treatment and follow-up. *Ann Oncol*. 2017;28:72–83.
- Siegel RL, Miller KD, Jemal A. Cancer statistics, 2019. *CA-Cancer J Clin*. 2019;69:7–34.
- Jin YJ, Kim SC, Kim HJ, Ju W, Kim YH, Kim HJ. Use of autoantibodies against tumor-associated antigens as serum biomarkers for primary screening of cervical cancer. *Oncotarget*. 2017;62:105425–39.
- Kaminska A, Sprynskyy M, Winkler K, Szymborski T. Ultrasensitive SERS immunoassay based on diatom biosilica for detection of interleukins in blood plasma. *Anal Bioanal Chem*. 2017;409:6337–47.
- Zhao QY, Duan RQ, Yuan JL, Quan Y, Yang H, Xi MR. A reusable localized surface plasmon resonance biosensor for quantitative detection of serum squamous cell carcinoma antigen in cervical cancer patients based on silver nanoparticles array. *Int J Nanomedicine*. 2014;9:1097–104.
- Zhou L, Liu Y, Wang FY, Jia ZJ, Zhou J, Jiang T, et al. Classification analyses for prostate cancer, benign prostate

- hyperplasia and healthy subjects by SERS-based immunoassay of multiple tumour markers. *Talanta*. 2018;188:238–44.
9. Zhou Y, Wang W, Wei R, Jiang GY, Li F, Chen X, et al. Serum bradykinin levels as a diagnostic marker in cervical cancer with a potential mechanism to promote VEGF expression via BDKRB2. *Int J Oncol*. 2019;55:131–41.
 10. Chon H, Lee S, Yoon SY, Chang SI, Lima DW, Choo J. Simultaneous immunoassay for the detection of two lung cancer markers using functionalized SERS nanotags. *Chem Commun*. 2011;47:12515–7.
 11. Cho HB, Hong SW, Oh YJ, Kim MA, Kang ES, Lee JM, et al. Clinical significance of osteopontin expression in cervical cancer. *J Cancer Res Clin Oncol*. 2008;134:909–17.
 12. Icer MA, Gezmen-Karadag M. The multiple functions and mechanisms of osteopontin. *Clin Biochem*. 2018;59:17–24.
 13. Xu Q, Yuan BB, Xue FX, Zhang LQ, Li J, Guo HL, et al. OPN gene polymorphisms are associated with susceptibility and clinicopathological characteristics of cervical cancer in a Chinese cohort. *Cancer Biomark*. 2011;10:233–9.
 14. Sharma P, Kumar S, Kundu GC. Transcriptional regulation of human osteopontin promoter by histone deacetylase inhibitor, trichostatin A in cervical cancer cells. *Mol Cancer*. 2010;9:178–90.
 15. Mua GY, Wang HJ, Cai ZG, Ji H. OPN -443C>T genetic polymorphism and tumor OPN expression are associated with the risk and clinical features of papillary thyroid cancer in a Chinese cohort. *Cell Physiol Biochem*. 2013;32:171–9.
 16. Cheng ZY, Choi N, Wang R, Lee S, Moon KC, Yoon SY, et al. Simultaneous detection of dual prostate specific antigens using surface-enhanced Raman scattering-based immunoassay for accurate diagnosis of prostate cancer. *ACS Nano*. 2017;11:4926–33.
 17. Wang ZY, Zong SF, Wu L, Zhu D, Cui YP. SERS-activated platforms for immunoassay: probes, encoding methods, and applications. *Chem Rev*. 2017;117:7910–63.
 18. Wang XK, Choi N, Cheng ZY, Ko JH, Chen LX, Choo J. Simultaneous detection of dual nucleic acids using a SERS-based lateral flow assay biosensor. *Anal Chem*. 2017;89:1163–9.
 19. Li XZ, Yang TY, Song YT, Zhu JH, Wang DL, Li W. Surface-enhanced Raman spectroscopy (SERS)-based immunochromatographic assay (ICA) for the simultaneous detection of two pyrethroid pesticides. *Sens Actuator B-Chem*. 2019;283:230–8.
 20. Zheng ZH, Wu L, Li L, Zong SF, Wang ZY, Cui YP. Simultaneous and highly sensitive detection of multiple breast cancer biomarkers in real samples using a SERS microfluidic chip. *Talanta*. 2018;188:507–15.
 21. Tian Y, Liu H, Chen Y, Zhou C, Jiang Y, Gu C, et al. Seedless one-spot synthesis of 3D and 2D Ag nanoflowers for multiple phase SERS-based molecule detection. *Sens Actuator B-Chem*. 2019;301:127–42.
 22. Zhao P, Li HX, Li DW, Hou YJ, Mao L, Yang M, et al. A SERS nano-tag-based magnetic-separation strategy for highly sensitive immunoassay in unprocessed whole blood. *Talanta*. 2019;198:527–33.
 23. Wang Z, Yang HQ, Wang MH, Petti LC, Jiang T, Jia ZH, et al. SERS-based multiplex immunoassay of tumor markers using double SiO₂@Ag immune probes and gold-film hemisphere array immune substrate. *Colloid Surf A-Physicochem Eng Asp*. 2018;546:48–58.
 24. Fales AM, Yuan H, Vo-Dinh T. Development of hybrid silver-coated gold nanostars for nonaggregated surface-enhanced Raman scattering. *J Phys Chem C*. 2014;118:3708–15.
 25. Lin S, Lin X, Liu YL, Zhao HY, Hasi W, Wang L. Self-assembly of Au@Ag core-shell nanocubes embedded with internal standard for reliable quantitative SERS measurements. *Anal Methods*. 2018;10:4201–8.
 26. Khlebtsov BN, Khanadeev VA, Tsvetkov MY, Bagratashvili VN, Khlebtsov NG. Surface-enhanced Raman scattering substrates based on self-assembled PEGylated gold and gold-silver core-shell nanorods. *J Phys Chem C*. 2013;117:23162–71.
 27. Tian YF, Zhou W, Yin BC, Ye BC. Highly sensitive surface-enhanced Raman scattering detection of adenosine triphosphate based on core-satellite assemblies. *Anal Methods*. 2017;9:6038–43.
 28. Tan LQ, Liu C, Wang Y, Sun J, Dong J, Qian WP. Fabrication of SERS substrates containing dense “hot spots” by assembling star-shaped nanoparticles on superhydrophobic surfaces. *New J Chem*. 2017;41:5028–33.
 29. Muhammad M, Shao CS, Huang Q. Label-free SERS diagnostics of radiation-induced injury via detecting the biomarker Raman signal in the serum and urine bio-samples based on Au-NPs array substrates. *Spectrosc Acta Pt A-Mol Biomol Spectr*. 2019;223:117282–92.
 30. Yoo J, Lee SW. Facile synthesis of silica-encapsulated gold nanoflowers as surface-enhanced Raman scattering probes using silane-mediated sol-gel reaction. *J Nanosci Nanotechnol*. 2016;16:6289–93.
 31. Zhou L, Han ST, Shu SW, Zhuang JQ, Yan Y, Sun QJ, et al. Localized surface plasmon resonance-mediated charge trapping/detrapping for core-shell nanorod-based optical memory cells. *ACS Appl Mater Interfaces*. 2017;9:34101–10.
 32. Bai TT, Sun JF, Che RC, Xu LN, Yin CY, Guo ZR, et al. Controllable preparation of core-shell Au-Ag nanoshuttles with improved refractive index sensitivity and SERS activity. *ACS Appl Mater Interfaces*. 2014;6:3331–40.
 33. Yi SJ, Sun LM, Lenaghan SC, Wang YZ, Chong XY, Zhang ZL, et al. One-step synthesis of dendritic gold nanoflowers with high surface-enhanced Raman scattering (SERS) properties. *RSC Adv*. 2013;3:10139–44.
 34. Sun G, Ye G, Wang K, Lou M, Jia X, Xu F, et al. Deposition of Ag films on liquid substrates via thermal evaporation for surface-enhanced Raman scattering. *ACS Omega*. 2020;5:7440–5.
 35. Bu Y, Lee SW. Flower-like gold nanostructures electrodeposited on indium tin oxide (ITO) glass as a SERS-active substrate for sensing dopamine. *Microchim Acta*. 2015;182:1313–21.
 36. Reokrungruang P, Chatnuntaweck I, Dharakul T, Bamrungsap S. A simple paper-based surface enhanced Raman scattering (SERS) platform and magnetic separation for cancer screening. *Sens Actuator B-Chem*. 2019;285:462–9.
 37. Xie J, Li LY, Khan IM, Wang ZP, Ma XY. Flexible paper-based SERS substrate strategy for rapid detection of methyl parathion on the surface of fruit. *Spectrosc Acta Pt A-Mol Biomol Spectr*. 2020;2231:118104–12.
 38. Linh VTN, Moon J, Mun CW, Devaraj V, Oh JW, Park SG, et al. A facile low-cost paper-based SERS substrate for label-free molecular detection. *Sens Actuator B-Chem*. 2019;291:369–77.
 39. Zhang CM, You TT, Yang N, Gao YK, Jiang L, Yin PG. Hydrophobic paper-based SERS platform for direct-droplet quantitative determination of melamine. *Food Chem*. 2019;287:363–8.
 40. Lee M, Oh K, Choi HK, Lee SG, Youn HJ, Lee HL, et al. Subnanomolar sensitivity of filter paper-based SERS sensor for pesticide detection by hydrophobicity change of paper surface. *Sensors*. 2018;3:151–9.
 41. Han CQ, Li YQ, Jia Q, Bradley LH, Gan Y, Yao Y, et al. On-demand fabrication of surface-enhanced Raman scattering arrays by pen writing, and their application to the determination of melamine in milk. *Microchim Acta*. 2017;184:2909–17.
 42. Lee DJ, Kim DY. Hydrophobic Paper-Based SERS. Sensor using gold nanoparticles arranged on graphene oxide flakes. *Sensors*. 2019;19:5471–80.
 43. Zhao H, Hasi W, Li N, Sha XY, Lina S, Han S. In situ analysis of pesticide residues on the surface of agricultural products via

- surface-enhanced Raman spectroscopy using a flexible Au@Ag-PDMS substrate. *New J Chem*. 2019;43:13075–82.
44. Li M, Zhang ZS, Zhang X, Li KY, Yu XF. Optical properties of Au/Ag core/shell nanoshuttles. *Opt Express*. 2008;18:14288–93.
 45. Liu K, Bai YC, Zhang L, Yang ZB, Fan QK, Zheng HQ, et al. Porous Au–Ag nanospheres with high-density and highly accessible hotspots for SERS analysis. *Nano Lett*. 2016;16:3675–81.
 46. Liu F, Lu YH, Yu WH, Fu Q, Wang P, Ming H. Tunable surface-enhanced Raman spectroscopy via plasmonic coupling between nanodot-arrayed Ag film and Ag nanocube. *Plasmonics*. 2013;8:1279–84.
 47. Baghbanian SM, Rezaei N, Tashakkorian H. Cheminform abstract: nanozeolite clinoptilolite as a highly efficient heterogeneous catalyst for the synthesis of various 2-amino-4H-chromene derivatives in aqueous media. *Green Chem*. 2014;15:3446–58.
 48. Qi W, Zhou DB, Chen SL, Huang Y, Cheng X. Preparation and electrocatalytic properties of Fe, Co, Ni-polymer-C complex catalysts for ethanol electro-oxidation. *Acta Chim Sin*. 2009;67:917–22.
 49. Nagase Y, Yoshida S, Kamiyama K. Analysis of human tear fluid by Fourier transform infrared spectroscopy. *Biopolymers*. 2005;79:18–27.
 50. Liu KZ, Shaw RA, Man A, Dembinski TC, Mantsch HH. Reagent-free, simultaneous determination of serum cholesterol in HDL and LDL by infrared spectroscopy. *Clin Chem*. 2002;48:499–506.
 51. Song CY, Yang YJ, Yang BY, Min LH, Wang LH. Combination assay of lung cancer associated serum markers using surface-enhanced Raman spectroscopy. *J Mater Chem B*. 2016;4:1811–7.

Publisher's note Springer Nature remains neutral with regard to jurisdictional claims in published maps and institutional affiliations.